Relativistic effects on tidal disruption kicks of solitary stars

E. Gafton,[1][★] E. Tejeda,[1] J. Guillochon,[2][†] O. Korobkin[1] and S. Rosswog[1]

[1]*The Oskar Klein Centre, Department of Astronomy, AlbaNova, Stockholm University, SE-106 91 Stockholm, Sweden*
[2]*Harvard–Smithsonian Center for Astrophysics, Institute for Theory and Computation, 60 Garden Street, Cambridge, MA 02138, USA*

ABSTRACT

Solitary stars that wander too close to their galactic centres can become tidally disrupted, if the tidal forces due to the supermassive black hole residing there overcome the self-gravity of the star. If the star is only partially disrupted, so that a fraction survives as a self-bound object, this remaining core will experience a net gain in specific orbital energy, which translates into a velocity 'kick' of up to $\sim 10^3$ km s^{-1}. In this paper, we present the result of smoothed particle hydrodynamics simulations of such partial disruptions, and analyse the velocity kick imparted on the surviving core. We compare $\gamma = 5/3$ and $\gamma = 4/3$ polytropes disrupted in both a Newtonian potential, and a generalized potential that reproduces most relativistic effects around a Schwarzschild black hole either exactly or to excellent precision. For the Newtonian case, we confirm the results of previous studies that the kick velocity of the surviving core is virtually independent of the ratio of the black hole to stellar mass, and is a function of the impact parameter β alone, reaching at most the escape velocity of the original star. For a given β, relativistic effects become increasingly important for larger black hole masses. In particular, we find that the kick velocity increases with the black hole mass, making larger kicks more common than in the Newtonian case, as low-β encounters are statistically more likely than high-β encounters. The analysis of the tidal tensor for the generalized potential shows that our results are robust lower limits on the true relativistic kick velocities, and are generally in very good agreement with the exact results.

Key words: black hole physics – hydrodynamics – relativistic processes – methods: numerical – galaxies: nuclei.

1 INTRODUCTION

The centres of most galaxies are hosts to supermassive black holes (SMBHs) with masses ranging from $\sim 10^5$ M$_\odot$ (Secrest et al. 2012) to as much as a few $\times 10^{10}$ M$_\odot$ (van den Bosch et al. 2012). The SMBH's mass is comparable to the combined mass of all the stars in the nucleus, and together they control the orbital dynamics of individual stars. Various mechanisms (the most important being two-body scattering; see e.g. Alexander 2005) may at times bring one of the stars on to a nearly radial orbit that reaches the immediate vicinity of the SMBH, with the periapsis distance r_p becoming comparable to the tidal radius $r_t \equiv (M_{bh}/m_\star)^{1/3} r_\star$ (Frank 1978). On average, this happens at a rate of $\sim 10^{-5}$ yr^{-1} per galaxy (Magorrian & Tremaine 1999; Wang & Merritt 2004). The strength of the encounter, quantified by the impact parameter $\beta \equiv r_t/r_p$, will ultimately determine how much mass the star loses due to tidal inter-

actions, whether it survives ($\beta \lesssim 1$) or is completely ripped apart ($\beta \gtrsim 1$) (Rees 1988).

Recent simulations by Manukian et al. (2013, henceforth MGRO; see Manukian et al. 2014 for errata) showed that in partial disruptions, in which a fraction of the star survives as a self-bound object, the remaining core may receive a boost in specific orbital energy, corresponding to a velocity 'kick' that can reach the surface escape velocity of the original star, and may later on be observed as a 'turbo-velocity star'. The source of this increase in energy has been linked to the asymmetry of the two tidal tails created during the disruption process, which by conservation of linear momentum boosts the velocity of the surviving core. This asymmetry (and the velocity kick it induces) appears to be an inherent property of tidal disruption events, and has also been observed in tidal disruptions of planets (Faber, Rasio & Willems 2005), white dwarfs (Cheng & Evans 2013) and neutron stars (Rosswog et al. 2000; Kyutoku, Ioka & Shibata 2013).

In this paper, we extend the previous results by performing smoothed particle hydrodynamics (SPH) simulations of tidal disruptions of solar-type stars by SMBHs. We use both a completely Newtonian approach and one where the orbital dynamics around a

Schwarzschild black hole is accurately reproduced by a generalized potential (Tejeda & Rosswog [2013], henceforth TR). Apart from a verification of the previous results with different numerical methods, our main goal is to quantify to which extent the relativistic effects from a Schwarzschild black hole would impact on the final velocities. The study of these events may contribute to the understanding of hypervelocity stars (HVSs; Hills [1988]), which were thought to result either from the tidal disruption of binary stars, or by scattering off the stellar-mass black holes segregated in the Galactic Centre (O'Leary & Loeb [2008]). While these processes can indeed impart velocities in excess of 10^3 km s^{-1} (Brown et al. [2005]; Antonini et al. [2010]), most observed HVSs seem to have rather modest velocities, typically around $\sim$400 km s^{-1} (e.g. Palladino et al. [2014]; Zheng et al. [2014]; Zhong et al. [2014]). A number of HVSs have even been observed on bound orbits around the Galactic Centre, but with sufficiently high velocities so as to constitute a distinct population of velocity outliers (Brown et al. [2007]). Tidal disruptions of solitary stars may therefore yield sufficiently large kicks to explain many of these HVSs, especially if the kicks are significantly enhanced by relativistic effects.

2 METHOD

In our simulations, we use the Newtonian SPH code described in detail by Rosswog, Ramirez-Ruiz & Hix ([2009]), with self-gravity computed using a binary tree similar to that of Benz et al. ([1990]). The tree accuracy parameter (i.e. the opening angle $\theta > H_B/R_{AB}$ which controls whether a distant tree node B, of size H_B and located at a distance R_{AB} from node A, is allowed to act as a multipole source of gravity for node A or needs to be further resolved into its constituents) was set to $\theta = 0.5$, corresponding to an average relative force error of $\lesssim 0.1$ per cent. All simulations use 10^5 SPH particles, unless otherwise stated (we verified the results via two runs with 10^6 particles).

We model stars as polytropic fluids with $\gamma = 5/3$, which initially satisfy the Lane–Emden equation for $m_\star = 1\,M_\odot$ and $r_\star = 1\,R_\odot$. It has long been known that $\gamma = 5/3$ polytropes are disrupted at smaller βs than $\gamma = 4/3$ polytropes, which, being more centrally condensed, are able to survive deeper encounters (see e.g. Guillochon & Ramirez-Ruiz [2013]). In order to compare our results with those of MGRO, who used $\gamma = 4/3$, we also perform a few test simulations in which the initial stellar profiles are given by $\gamma = 4/3$ polytropes, but the fluid, being gas-pressure dominated, reacts to dynamical compressions and expansions according to a $\gamma = 5/3$ equation of state.

The black hole gravity is modelled with both the Newtonian potential ('Φ_N') and the generalized Newtonian potential ('Φ_{TR}'; TR),

$$\Phi_{TR}(r, \dot{r}, \dot{\varphi}) = -\frac{GM_{bh}}{r} - \frac{1}{2}\left(\frac{r_s}{r - r_s}\right)\left[\left(\frac{2r - r_s}{r - r_s}\right)\dot{r}^2 + r^2\dot{\varphi}^2\right], \tag{1}$$

where $r_s = 2\,GM_{bh}/c^2$ is the Schwarzschild radius. The potential is based on an expansion of the relativistic equations of motion in the low-energy limit, without necessarily implying low-velocities or weak field. It has been shown to reproduce essentially all relevant orbital properties around a Schwarzschild black hole either exactly or to a very high degree of accuracy.

In the TR potential, the specific relativistic orbital energy ϵ_{TR} is computed as

$$\epsilon_{TR} = \frac{1}{2}\left[\frac{r^2\dot{r}^2}{(r - r_s)^2} + \frac{r^3\dot{\varphi}^2}{r - r_s}\right] - \frac{GM_{bh}}{r}. \tag{2}$$

The self-bound mass is calculated using the iterative energy-based approach described by Guillochon & Ramirez-Ruiz ([2013], section 2.2), with the gravitational self-potential calculated using a fast binary tree (Gafton & Rosswog [2011]). The kick velocity of the self-bound object (at infinity) is then computed as

$$v_{kick} = \sqrt{2(\epsilon - \epsilon_0)}, \tag{3}$$

where ϵ_0 is the specific orbital energy of the initial star at the beginning of the simulation, and ϵ is the specific orbital energy of the self-bound remnant. This definition does not take into account the underlying galactic gravitational potential, and therefore the kick velocity is expected to decrease as stars 'climb' out of the galactic potential.

Since we are only considering parabolic orbits, ϵ_0 is approximately equal to zero, with small numerical deviations due to the fact that only the centre of mass is on a truly parabolic orbit, since we impart the same initial orbital velocity to all particles, while starting with the star at an initial distance of $5\,r_t$ from the black hole, instead of at infinity.

We simulate encounters with mass ratios $q \equiv M_{bh}/m_\star$ in the range $10^6 \leq q \leq 4 \times 10^7$, and impact parameters β in the range $0.6 \leq \beta \leq 0.9$. For the $\gamma = 4/3$ runs, we use the same values of β and q as MGRO, namely 1.0–1.8, and 10^3–10^6, respectively. The values for β are chosen so that a self-bound core always survives, while q is chosen so that the star is disrupted outside the Schwarzschild radius of the SMBH.

A summary of all the simulations performed for this paper is presented in Table 1.

3 RESULTS

3.1 Disruption dynamics

The typical evolution of the stellar fluid during a partial tidal disruption is shown in Fig. 1. As it approaches periapsis, the star is heavily spun-up and distorted, being stretched in the radial direction, corresponding to the one positive eigenvalue of the tidal tensor, and compressed in the azimuthal and vertical directions (see Luminet & Carter [1986]; see also Appendix A for a discussion on the tidal tensor). As the star overfills its Roche lobe it starts to shed mass through the Lagrangian points L1 and L2, forming a bound and an unbound (to the SMBH) tail, respectively. As the star is receding from the black hole, the tails and the core stop exchanging energy and angular momentum (i.e. the energies become 'frozen-in') and the core recollapses into a self-bound, spherical object.

Fig. 2 shows the locations of the SPH particles in the time-varying Roche potential with respect to the centre of mass of the star (Ψ_{Roche}, see Appendix B for a derivation), calculated along the radial direction (upper row) and contours of Ψ_{Roche} in the orbital plane (lower row). The formation of the two tidal tails is asymmetric from the beginning (the star first overflows its Roche lobe through L1), but it is most clearly seen in panel (d$_2$). It is interesting to observe that in panel (b$_2$), representative of the star during the actual disruption, the Roche potential is not aligned with the star, i.e. the points through which the star sheds mass are not always aligned

Table 1. Overview of the SPH simulations discussed in this paper, grouped into three categories: 59 core simulations (1–59) with $\gamma = 5/3$ and 10^5 SPH particles, covering the entire range of q and β discussed in the paper; 25 test simulations (60–84) with $\gamma = 5/3$ (of which 24 with 10^6 SPH particles, and 1 with $\theta = 0.2$); 21 test simulations (85–105) with $\gamma = 4/3$. For each simulation, we show the polytropic index γ, the number of SPH particles N_{part}, the ratio $q = M_{bh}/m_\star$, the potential Φ (which is either the Newtonian potential, Φ_N, or the generalized Newtonian (TR) potential, Φ_{TR}) and the impact parameter $\beta = r_t/r_p$.

| Number	γ	N_{part}	q	Φ	θ	β
1–7	5/3	10^5	10^6	Φ_N	0.5	0.60, 0.65, 0.70, 0.75, 0.80, 0.85, 0.90
8–16	5/3	10^5	10^6	Φ_{TR}	0.5	0.60, 0.65, 0.70, 0.75, 0.80, 0.85, 0.88, 0.89, 0.90
17–23	5/3	10^5	4×10^6	Φ_N	0.5	0.60, 0.65, 0.70, 0.75, 0.80, 0.85, 0.90
24–31	5/3	10^5	4×10^6	Φ_{TR}	0.5	0.60, 0.65, 0.70, 0.75, 0.80, 0.83, 0.84, 0.85
32–38	5/3	10^5	10^7	Φ_N	0.5	0.60, 0.65, 0.70, 0.75, 0.80, 0.85, 0.90
39–45	5/3	10^5	10^7	Φ_{TR}	0.5	0.60, 0.65, 0.70, 0.75, 0.77, 0.78, 0.80
46–52	5/3	10^5	4×10^7	Φ_N	0.5	0.60, 0.65, 0.70, 0.75, 0.80, 0.85, 0.90
53–59	5/3	10^5	4×10^7	Φ_{TR}	0.5	0.60, 0.65, 0.68, 0.70, 0.71, 0.72, 0.75
60–66	5/3	10^6	10^6	Φ_N	0.5	0.60, 0.65, 0.70, 0.75, 0.80, 0.85, 0.90
67–73	5/3	10^6	10^6	Φ_{TR}	0.5	0.60, 0.65, 0.70, 0.75, 0.80, 0.85, 0.90
74–75	5/3	10^6	4×10^6	Φ_{TR}	0.5	0.83, 0.84
76	5/3	10^6	10^7	Φ_N	0.5	0.70
77	5/3	10^6	10^7	Φ_{TR}	0.5	0.70
78–83	5/3	10^6	4×10^7	Φ_{TR}	0.5	0.60, 0.65, 0.67, 0.70, 0.71, 0.72
84	5/3	10^5	10^7	Φ_{TR}	0.2	0.70
85	4/3	10^6	10^4	Φ_{TR}	0.5	1.60
86	4/3	10^6	10^6	Φ_{TR}	0.5	1.30
87–91	4/3	10^5	10^6	Φ_{TR}	0.5	1.45, 1.55, 1.65, 1.75, 1.80
92–95	4/3	10^5	10^6	Φ_N	0.5	1.45, 1.55, 1.65, 1.75
96–100	4/3	10^5	4×10^6	Φ_N	0.5	1.10, 1.20, 1.30, 1.70, 1.80
101–105	4/3	10^5	4×10^6	Φ_{TR}	0.5	1.10, 1.20, 1.30, 1.65, 1.70
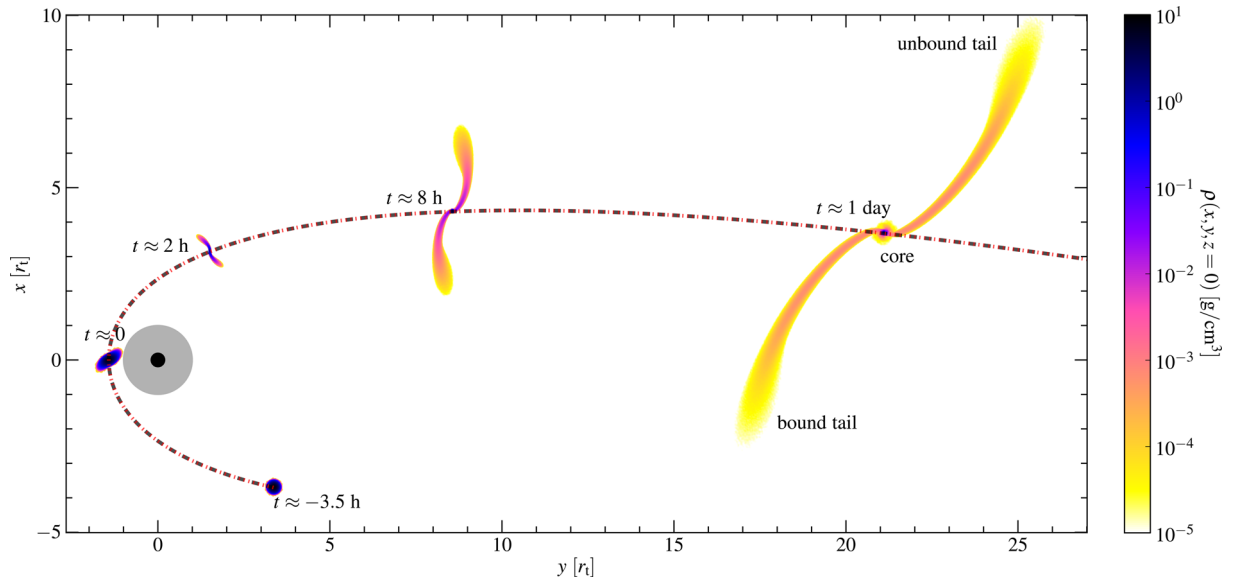
Figure 1. Evolution of the stellar fluid during a typical, parabolic partial tidal disruption. The plot shows a cross-section of the density profile in the orbital plane ($z = 0$). Here, $N_{part} = 10^6$, $q = 10^7$, $\beta = 0.7$ and $\Phi = \Phi_{TR}$. The Schwarzschild radius (black disc), tidal radius (grey disc), geodesic trajectory of the centre of mass in Schwarzschild space–time (dotted red line) and trajectory of the centre of mass obtained with the TR potential (dashed black line) are shown to scale. Due to the spatial scales involved, we show the stellar debris magnified by a factor of 50 before periapsis passage ($t \leq 0$) and magnified by a factor of 10 afterwards ($t > 0$). Note that due to relativistic periapsis shift the orbit is not a parabola.

with the instantaneous L1 and L2. This occurs because the orbital time-scale of the system is shorter than the dynamical time-scale on which the fluid can react to the extremely fast-changing Roche potential ($\tau_{orb} < \tau_{dyn}$).

3.2 Self-bound mass

The self-bound mass fraction evolves during the disruption process, and for a partial disruption it will decrease from 1 (before disruption, when the entire star is self-bound) to the final value $m_{core}/m_\star$. In
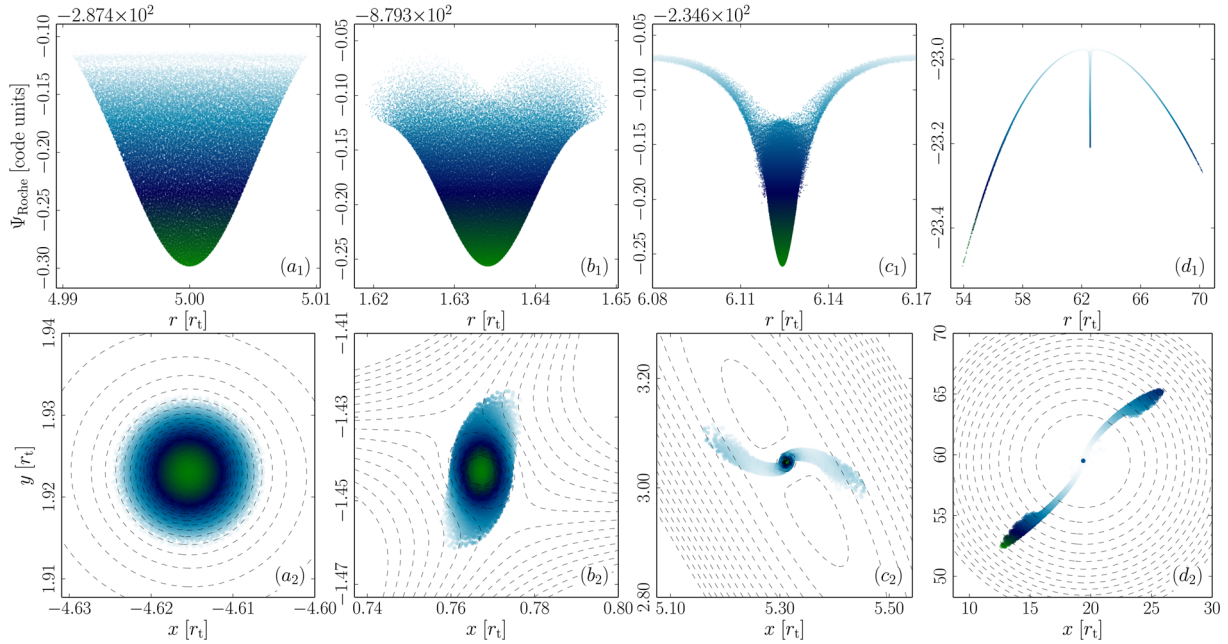
Figure 2. A typical, time-varying Roche potential in a partial tidal disruption exhibits a number of stages, shown here as snapshots at: (a) $t \approx -3.5$ h before periapsis passage, i.e. at the beginning of the simulation, when the star is self-bound; (b) $t \approx 20$ min, just as the first particles exit the Roche lobe of the star and start forming the tidal tails (bound tail first); (c) $t \approx 4$ h, as the energy distribution of the debris starts to freeze and the core and tails approach their final masses; (d) $t \approx 4$ d after the disruption. This simulation used $N_{part} = 10^5$, $q = 10^6$, $\beta = 0.65$ and $\Phi = \Phi_N$. Upper row. $\Psi_{Roche}(r)$, where r is the distance to the SMBH. The values of Ψ_{Roche} are given in code units and – to simplify axis labelling – are offset by the values shown in the upper-left corner of the panels. Lower row. Contours of $\Psi_{Roche}(x, y)$ in the orbital plane, with the particles overplotted and coloured according to the value of the potential. All coordinate axes use a global Cartesian coordinate system, with the SMBH always located at (0, 0, 0), and the stellar fluid moving along a parabolic orbit around it. In the lower row, we are essentially 'zooming in' on the SPH particle distribution as it first approaches, and then recedes from the SMBH.
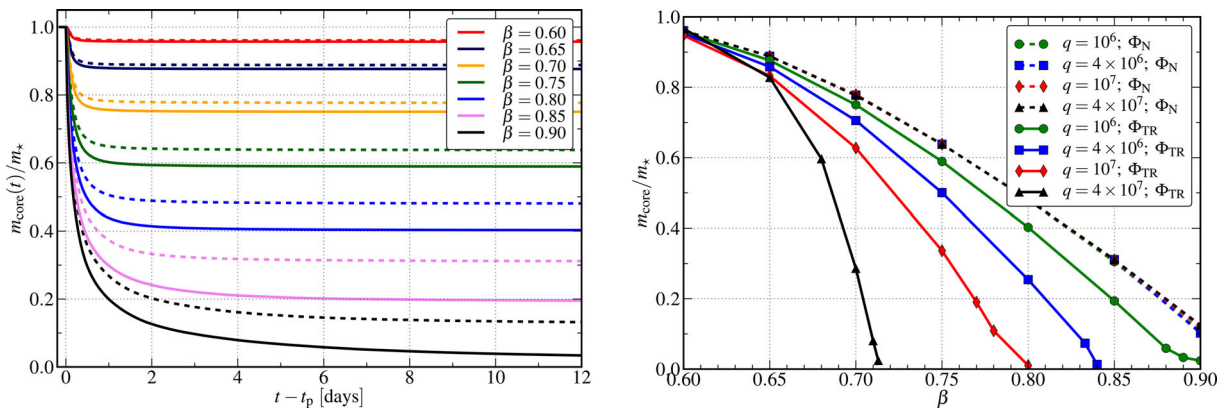

Figure 3. Left-hand panel. Evolution of the self-bound mass fraction in simulations using Newtonian (dashed lines) and TR (solid lines) potentials. Right-hand panel. Final self-bound mass fraction in Newtonian (dashed lines) and TR (solid lines) simulations. The points corresponding to Newtonian runs are essentially overlapping for all values of β, while those from pseudo-relativistic simulations show a strong dependence on q: the larger q is, the smaller the critical β necessary for complete disruption is.

Fig. 3 (left-hand panel), we present the time-evolution of m_{core} for the $q = 10^6$ simulations. The disruption is stronger in relativistic encounters, with the deviation of the self-bound mass fraction from the Newtonian case increasing with β, from $\sim$ few per cent ($\beta = 0.6$) to ~ 100 per cent ($\beta = 0.9$).

Fig. 3 (right-hand panel) shows the final self-bound mass fraction as a function of β, for various ratios q and for both potentials. We observe that with the Newtonian potential stars are partially disrupted in the range $0.6 \lesssim \beta \lesssim 0.9$ regardless of q. This result is general for all Newtonian disruptions of $\gamma = 5/3$ polytropes, and agrees with the numerical findings of e.g. Guillochon & Ramirez-Ruiz (2013)

(β_d necessary for complete disruption equal to 0.9). On the other hand, for any given β the discrepancy between Newtonian and TR simulations increases drastically for larger black hole masses, as r_s becomes comparable to r_p and relativistic terms in the tidal tensor close to periapsis can no longer be ignored (see Appendix A).

3.3 Kick velocity

The kick velocity is computed from the increase in specific orbital energy ($\epsilon - \epsilon_0$) of the self-bound core using equation (3). In Fig. 4, we present v_{kick} both as a function of time for the
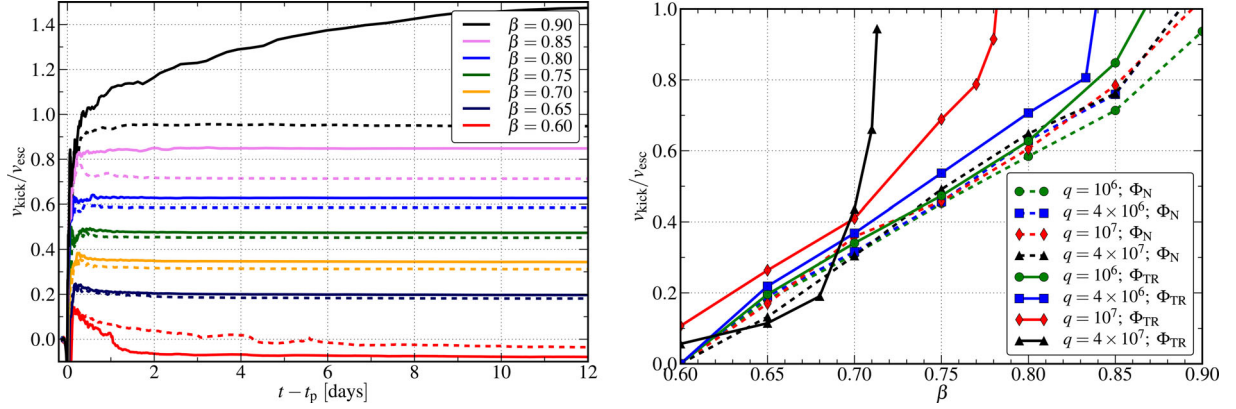
Figure 4. Left-hand panel. Evolution of the kick velocity of the self-bound remnant in Newtonian (dashed lines) and TR (solid lines) simulations. The kick velocity is normalized by the surface escape velocity of a solar-type star, ≈ 617 km s^{-1}. The lines show a moving average of the data points in order to smooth out fluctuations during the disruption process (before the surviving remnant becomes relaxed, i.e. approximately during $t = 0$ and $t = 1$). Right-hand panel. Kick velocity of the self-bound remnant at infinity, in Newtonian (dashed lines) and TR (solid lines) simulations. The solid black line ($q = 4 \times 10^7$, $\Phi = \Phi_{TR}$) stands out, as for low values of β it surprisingly falls both below the runs with smaller q, and below the Newtonian run. We have repeated this set of simulations with higher resolution (10^6 SPH particles), but the results were very similar. Since these are highly relativistic encounters, further studies with even higher resolution and an exact relativistic treatment of the black hole gravity are probably required in order to arrive at a definitive answer..

$q = 10^6$ simulations (left-hand panel), and its final value at the end of the simulation (right-hand panel). The kick velocities are always scaled to the surface escape velocity of the original star, $\sqrt{2GM_\odot/R_\odot} \approx 617$ km s^{-1}, as they are expected to be comparable on theoretical grounds (see Manukian et al. 2013).

We initially place the star at $5\,r_t$, and observe that numerical deviations from $\epsilon_0 = 0$ (i.e. parabolic trajectory) of the initial specific energy increases with q, and is larger for the TR potential. For the most extreme case ($q = 4 \times 10^7$, $\beta = 0.9$, Φ_{TR}), the initial energy was of the order of $\sim 10^{-8}c^2$ (which is to be compared with the typical 'kick' specific energy, $\sim 10^{-6}c^2$), while for the other simulations it was between one and three orders of magnitude smaller (for the TR and Newtonian potentials, respectively). Nevertheless, there is a clear distinction between the Newtonian runs, where the kick is fairly independent of q, and the TR runs, where the curves exhibit an asymptotic behaviour limited by progressively smaller βs with larger q's.

The time evolution of ϵ and – consequently – of v_{kick} exhibits significant oscillations during the actual disruption ($\sim$ hours from periapsis passage) that appear as wiggles in Fig. 4. The explanation is likely related to the complicated hydrodynamic effects that take place in that short period of time. Due to the extreme compression of the star, shock waves travel throughout the star and transfer significant energy and angular momentum between the particles, and until the energies become frozen-in, the average specific energy of the bound core keeps oscillating.

Fig. 5 shows the kick velocity as a function of the self-bound mass fraction m_{core}. We notice that in contrast to the findings of MGRO, in some simulations the kick velocity exceeds the escape velocity of the initial star, but only when the value of m_{core} is sufficiently small. Indeed, $v_{kick}(m_{core})$ seems to be a monotonic function that asymptotically approaches 0 for $m_{core} \to m_\star$ and $+\infty$ for $m_{core} \to 0$.

Fig. 6 shows the kick velocity as a function of the mass difference between the two tidal tails, Δm_{12} (Fig. 6, left- and right-hand panels, for Newtonian and TR potentials, respectively). The two plots exhibit similar behaviours (v_{kick} increases with Δm_{12}), but in the relativistic simulations the degeneracy in q is broken (i.e. the
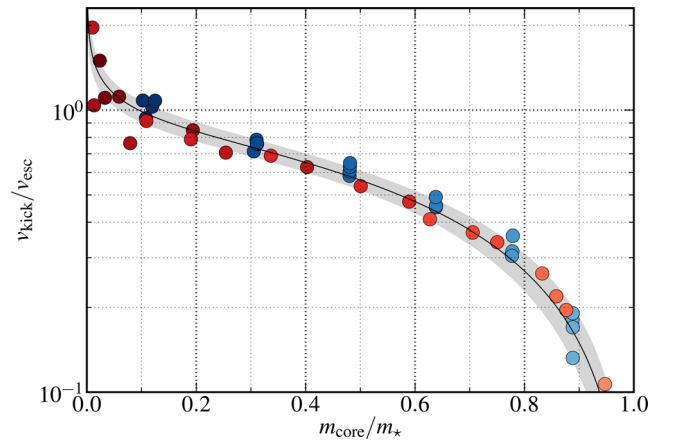

Figure 5. The kick velocity v_{kick} of the self-bound remnant shows a remarkable dependence on the self-bound mass fraction in both Newtonian (blue points) and TR (red points) simulations. We fitted a truncated power law of the form $y = Ax^{-a}(1 - x^2)^b$, with the fit parameters $A = 0.634\,726$, $a = 0.196\,598$, $b = 0.882\,387$. The shaded grey area around the black fit line represents the 1σ deviation from the fit. Darker points correspond to higher values of β.

data points for a given β are not clustered together irrespective of q), since the relativistic kicks are sensitive to both β and q.

We also show v_{kick} as a function of β for the $\gamma = 4/3$ simulations (Fig. 7), together with the fit line given by MGRO. These simulations show reasonable similarity to the results of MGRO, and – as expected – for such small values of q (10^3 to 10^6) there is little difference between Newtonian and TR simulations. The data points from our simulations give slightly smaller kicks than the fit, but the general trend (and critical β) are nevertheless recovered.

3.4 Error estimation and resolution dependence

Since in this paper we are concerned with parabolic encounters, we have calculated the TR acceleration for particles on parabolic orbits. It turns out that the TR potential reproduces parabolic orbits exactly
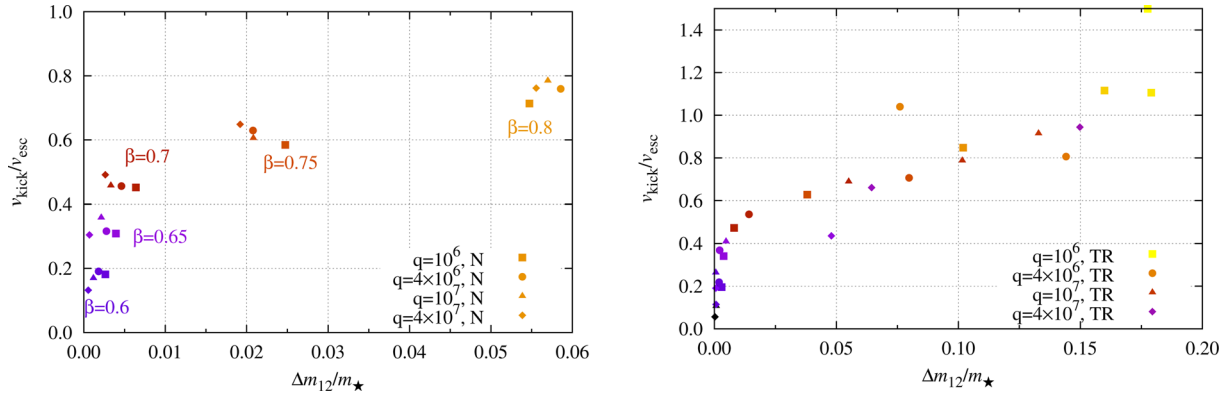
Figure 6. Kick velocity of the self-bound remnant as a function of the mass difference Δm_{12} between the tidal tails in Newtonian (left-hand panel) and TR (right-hand panel) simulations. The value of β is colour-coded. The relativistic results do not exhibit such a strong relation between β, Δm_{12}, and v_{kick} as in the case of the Newtonian potential, but they still obey the general trend (v_{kick} increases with Δm_{12}) and even the shape of the function.
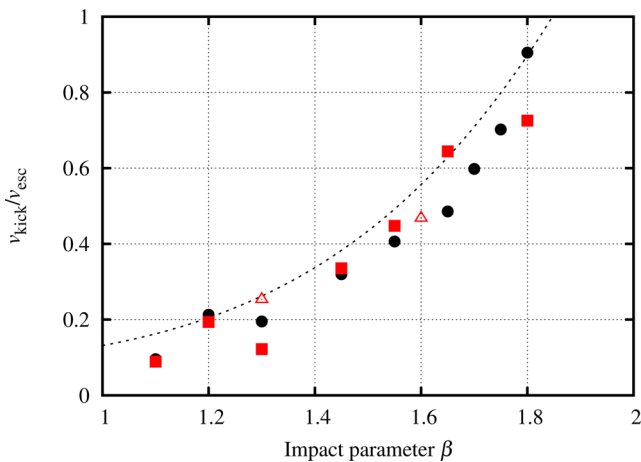

Figure 7. The results of our SPH simulations of $\gamma = 4/3$ polytropes, using $N_{part} = 10^5$ in Newtonian (black circles) and TR (red squares) potentials, and using $N_{part} = 10^6$ with the TR potential (red triangles), as compared to the fit line given by MGRO for their $\gamma = 4/3$ simulations. Our runs use the same values for q as in their paper (10^3–10^6), and for this reason relativistic effects are small.

(see TR; in our simulations, these would be the orbits of the centre of mass). In Fig. 8, we show the tidal deformation experienced by test particles placed on a ring of radius $4\,R_\odot$ with the centre following a parabolic orbit with $\beta = 1.6$ around a $10^7\,M_\odot$ black hole. The deformation of the ring provides a visual representation of the effects of the tidal tensor, and by eye it appears to be identical in Schwarzschild and Φ_{TR}. In Appendix A, we calculate in detail the components and the eigenvalues of the tidal tensor in Schwarzschild and both Newtonian and TR potentials, and show that the eigenvalues λ_2 and λ_3 (corresponding to compression in the orbital plane and perpendicular to it, respectively) provided by the TR potential for parabolic orbits are the same as in Schwarzschild (with λ_3 having an identical expression, and λ_2 having a slightly different expression that still gives the same result within machine precision for our range of parameters), while the maximum relative error in λ_1 (corresponding to expansion in the radial direction) is 6.4 per cent, occurring at periapsis for a very narrow range of βs. In general, the average error in λ_1 at periapsis is of the order of $\sim$ a per cent, and quickly drops farther away from the black hole. We also show that both the Newtonian and the TR potentials *always underestimate* the

values of λ_1 and λ_2, which means that all disruptions will be slightly stronger in the Schwarzschild space–time, leaving a smaller self-bound core and resulting in even larger velocity kicks. Therefore, our results are robust lower limits on the true relativistic effects.

We have also performed a number of test simulations with higher resolution. For $q = 10^6$, we ran all simulations with both 10^5 and 10^6 SPH particles; a comparison of the resulting kick velocities is presented in Fig. 9. The most striking observation is that resolution is crucial at low β ($\sim$0.6), where the mass asymmetry between the two tidal tails, which drives the kick, is extremely small, $\lesssim 10^{-2}\,m_\star$. This mass loss must be properly resolved in order for the kick effect to be accurately captured; we observe the low-resolution simulations greatly underestimate the kick for $\beta = 0.6$, due to more energy being deposited into the oscillation modes of the star. Resolution is also important, though not as crucial, at high β ($\sim$0.9), where the surviving core itself is of the order of $\sim 10^{-2}\,m_\star$, and must also be properly resolved; we observe that here the discrepancy between Φ_N and Φ_{TR} is less extreme for the higher resolution simulations, but this is simply because Φ_{TR} leaves a small surviving core, which is not resolved by the low-resolution simulations. For intermediate values of β, where both the core and the mass difference of the tails are a generous fraction of the initial stellar mass, lower-resolution simulations agree to a reasonable accuracy ($\sim$ few per cent) with the results obtained with the 10^6 particles simulations.

For $q = 10^7$, we ran the simulation with $\beta = 0.7$ with various numbers of SPH particles N_{part} and tree opening angles θ: for Φ_N, $N_{part} = 10^5$ and $N_{part} = 10^6$ (both with $\theta = 0.5$), and for Φ_{TR}, $N_{part} = 10^5$ ($\theta = 0.2, 0.5$), and $N_{part} = 10^6$ ($\theta = 0.5$). We observe that improving the force accuracy above $\theta = 0.5$ does not have a significant impact on the final kick velocity (at most $\sim$1 per cent), while increasing the number of particles ten times does change it by up to $\sim$10 per cent, for both potentials. In addition, the evolution of ϵ_{kick} during the disruption process is highly dependent on the resolution, with larger wiggles in the high-resolution simulations, presumably due to the fact that shocks are better resolved and therefore less dissipative, and there is significantly more energy transfer between the particles. Still, the difference between the kick velocities of the Newtonian and TR potentials is consistently and significantly larger than the variations that appear when changing the accuracy parameters for the same potential.

For $\gamma = 4/3$, we ran two additional simulations with $N_{part} = 10^6$ and $\Phi = \Phi_{TR}$, using $q = 10^4$, $\beta = 1.6$ and $q = 10^6$, $\beta = 1.3$. The kicks obtained in these higher-resolution simulations are shown in
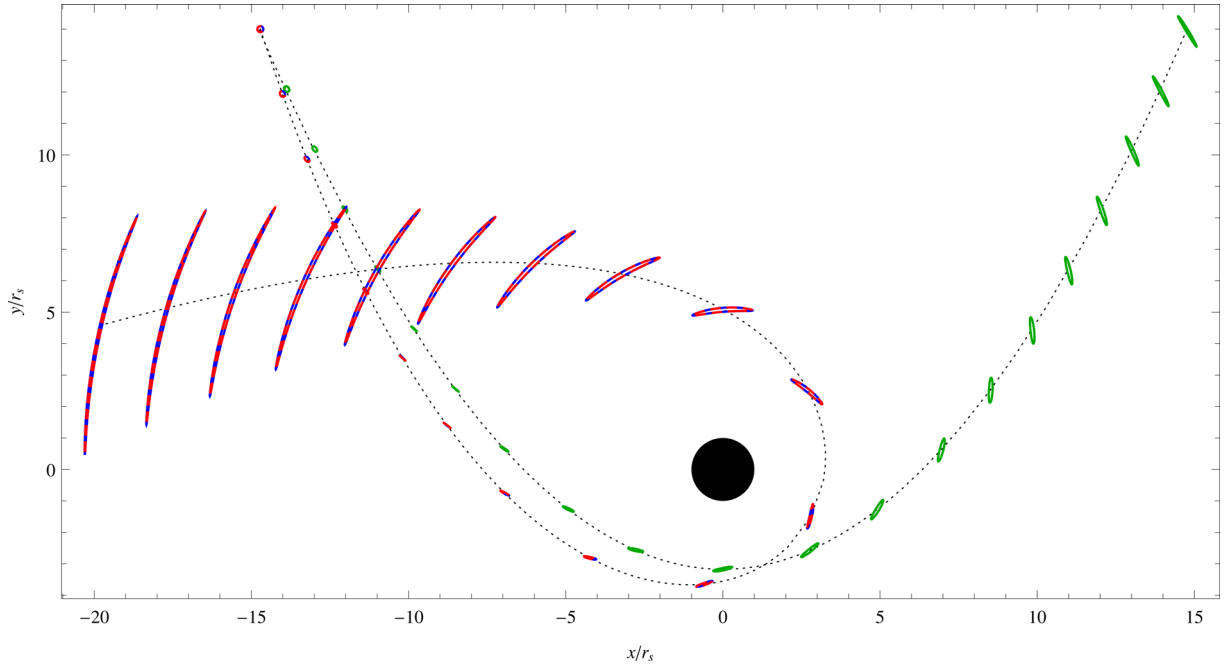
Figure 8. Visual representation of the tidal deformation experienced by a ring of particles of radius $4\,R_\odot$ (representing a star disrupted on a parabolic orbit with $\beta = 1.6$ by a SMBH with $q = 10^7$) in Schwarzschild space–time (red), the TR potential (blue) and the Newtonian potential (green). The rings in Schwarzschild space–time and the TR potential are indistinguishable from each other by eye, which is an indication that Φ_{TR} reproduces the Schwarzschild tidal tensor to a very good accuracy (see Appendix A for a further discussion). Unlike in the Newtonian case, where the shape of the rings would not change significantly after they exit the tidal radius, the other two rings become increasingly deformed due to the different periapsis shifts of their component particles (the TR potential reproduces the periapsis shift exactly).
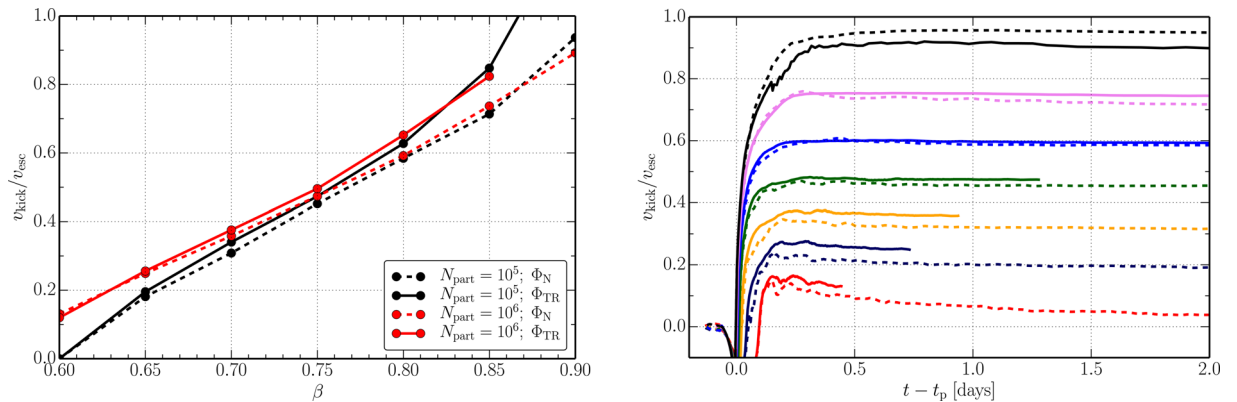

Figure 9. Left-hand panel. Kick velocity as a function of impact parameter β, obtained with lower ($N_{part} = 10^5$; black lines) and higher ($N_{part} = 10^6$; red lines) resolution simulations, representing both Φ_N (dashed lines) and Φ_{TR} (solid lines) encounters. Resolution appears to be critical at low β (~ 0.6), where the mass asymmetry of the two tails must be properly resolved in order to extract an accurate kick velocity (nevertheless, at both resolutions there is a clear trend of higher kick velocities in the relativistic case, compared to the Newtonian case). For the central part of the range, simulations with the two resolutions agree to within ~ 1 per cent. At large β, close to the critical impact parameter (~ 0.9), the two results agree for $\Phi = \Phi_N$, but for the TR encounter the 10^6 particles simulation results in no surviving core, while the 10^5 particles simulation still yields a small self-bound mass that acquires all the energy, resulting in a very large kick. Right-hand panel. Time evolution of the kick velocity for $q = 10^6$, $\Phi = \Phi_{TR}$ and $N_{part} = 10^5$ (dashed lines) and $N_{part} = 10^6$ (solid lines). The different colours represent different values of β. The best agreement between the kick velocities is achieved in the region of intermediate β, where both the mass asymmetry of the two tails and the surviving core are resolved in the lower-resolution runs. Since a significant fraction of the star survives for low βs, it is very expensive to run these simulations with high resolution, and therefore they were stopped at an earlier physical time than the high β simulations.

Fig. 7 with red squares, and are in good agreement with both the fit given by MGRO and the rest of the points from our simulations.

4 DISCUSSION

We have confirmed by a different numerical method (SPH versus the adaptive mesh refinement code FLASH that is primarily used

by MGRO) that all Newtonian simulations with the same impact parameter β produce similar self-bound remnants (in mass, specific energy and kick velocity), confirming earlier conclusions by Manukian et al. (2013) that v_{kick} is virtually independent of the mass ratio q.

We compared these calculations with simulations that use a generalized potential that accurately captures the dynamics around a

Schwarzschild black hole. Unlike Newtonian tidal disruptions, we observe that relativistic disruptions are no longer fully described by the parameter β. Instead, relativistic effects related to the tidal tensor become important when the periapsis distance is comparable to the Schwarzschild radius, i.e. they depend on the ratio

$$\Theta \equiv \frac{r_s}{r_p} = \beta \frac{m_\star}{r_\star} q^{2/3} \frac{2G}{c^2} \approx 0.2 \times \frac{\beta}{5} \left(\frac{r_\star}{R_\odot} \right)^{-1} \frac{m_\star}{M_\odot} \left(\frac{q}{10^6} \right)^{2/3}. \tag{4}$$

For a given mass ratio q, this can be interpreted as a dependence on β (e.g. for $q = 10^6$, relativistic effects become important when $\beta \gtrsim 5$, as noticed by e.g. Laguna et al. 1993), which will however change with q (for $q = 10^7$ relativistic effects are extremely important even for $\beta \lesssim 1$), since the gravitational radius and the tidal radius have different dependencies on M_{bh}. In general, we observe that relativistic effects can be ignored for $\Theta \lesssim 10^{-2}$ (where the relativistic and the Newtonian tidal tensor are essentially the same, and relativistic effects such as periapsis shift are negligible on the time-scale of the disruption), but tend to dominate the outcome of the encounter for $\Theta \gtrsim 0.1$. These thresholds can also be observed in Fig. A1 in the Appendix A, where we see that in a typical tidal disruption the eigenvalues of the tidal tensor are virtually identical in Newton and Schwarzschild for $r \gtrsim 30\, r_s$ and start to differ significantly from each other for $r \lesssim 10\, r_s$ (the exact values will of course depend on the parameters of the encounter).

We therefore expect relativistic effects on the kick velocity of turbo-velocity stars to be significant for larger black hole masses. In particular, since these objects will only result from partial disruptions ($0.6 \lesssim \beta \lesssim 0.9$, with the more pronounced velocity kicks at the higher end of this range), relativistic effects should dominate for $\Theta \gtrsim 0.1$, or, from equation (4), for

$$q \gtrsim 4.2 \times 10^6 \left(\frac{m_\star}{M_\odot} \right)^{-3/2} \left(\frac{r_\star}{R_\odot} \right)^{3/2}. \tag{5}$$

This means that for a solar-type star disrupted in our Galactic Centre relativistic effects may be important. In Fig. 4, we observe that for $q = 4 \times 10^6$ the TR potential will yield the same kick velocity as the Newtonian potential at an $\sim$5 per cent smaller β. Since tidal disruption rates scale with $\sim\beta^{-2}$ we estimate that approximately $\sim$10 per cent more stars will have a given kick velocity compared to a Newtonian estimation.

Previous estimations by Kesden (2012a,b) predict that the spin of the black hole may alter the spread in energy by up to a factor of $\sim$2. If one were to anticipate the relativistic effects due to the black hole spin, one would therefore expect a maximum of $\sim$40 per cent increase in the kick velocity, depending on the spin and orbit orientation, though a methodical study of such effects is left for subsequent investigations.

To conclude, we have found that the critical β necessary for the disruption of the star is highly dependent on q as long as $\Theta \gtrsim 10^{-2}$, with the star being completely disrupted at a β of around 0.9 ($q = 10^6$), 0.85 ($q = 4 \times 10^6$), 0.8 ($q = 10^7$), 0.72 ($q = 4 \times 10^7$), due to the proximity to the event horizon ($\Theta \approx 0.04$, 0.09, 0.16 and 0.36, respectively). This implies that the higher q is, the smaller the span of βs in which partial disruption will occur, and the steeper the dependence of the surviving core's mass, m_{core} on β is (Fig. 3). Since we have also shown that there is a very clear, monotonic relation between m_{core} and the kick velocity v_{kick} imparted to the core (Fig. 5), we conclude that – in Schwarzschild space–time – heavier black holes are able to impart larger kick velocities without requiring very deep encounters.

REFERENCES

Alexander T., 2005, Phys. Rep., 419, 65
Antonini F., Faber J., Gualandris A., Merritt D., 2010, ApJ, 713, 90
Benz W., Cameron A. G. W., Press W. H., Bowers R. L., 1990, ApJ, 348, 647
Brassart M., Luminet J.-P., 2008, A&A, 481, 259
Brassart M., Luminet J.-P., 2010, A&A, 511, A80
Brown W. R., Geller M. J., Kenyon S. J., Kurtz M. J., 2005, ApJ, 622, L33
Brown W. R., Geller M. J., Kenyon S. J., Kurtz M. J., Bromley B. C., 2007, ApJ, 660, 311
Cheng R. M., Evans C. R., 2013, Phys. Rev. D, 87, 104010
Faber J. A., Rasio F. A., Willems B., 2005, Icarus, 175, 248
Frank J., 1978, MNRAS, 184, 87
Gafton E., Rosswog S., 2011, MNRAS, 418, 770
Guillochon J., Ramirez-Ruiz E., 2013, ApJ, 767, 25
Hills J. G., 1988, Nature, 331, 687
Kesden M., 2012a, Phys. Rev. D, 85, 024037
Kesden M., 2012b, Phys. Rev. D, 86, 064026
Kyutoku K., Ioka K., Shibata M., 2013, Phys. Rev. D, 88, 041503
Laguna P., Miller W. A., Zurek W. H., Davies M. B., 1993, ApJ, 410, L83
Luminet J.-P., Carter B., 1986, ApJS, 61, 219
Magorrian J., Tremaine S., 1999, MNRAS, 309, 447
Manukian H., Guillochon J., Ramirez-Ruiz E., O'Leary R. M., 2013, ApJ, 771, L28
Manukian H., Guillochon J., Ramirez-Ruiz E., O'Leary R. M., 2014, ApJ, 782, L13 (MGRO)
Marck J.-A., 1983, Proc. R. Soc. A, 385, 431
O'Leary R. M., Loeb A., 2008, MNRAS, 383, 86
Palladino L. E., Schlesinger K. J., Holley-Bockelmann K., Allende Prieto C., Beers T. C., Lee Y. S., Schneider D. P., 2014, ApJ, 780, 7
Rees M. J., 1988, Nature, 333, 523
Rosswog S., Davies M. B., Thielemann F.-K., Piran T., 2000, A&A, 360, 171
Rosswog S., Ramirez-Ruiz E., Hix W. R., 2009, ApJ, 695, 404
Secrest N. J., Satyapal S., Gliozzi M., Cheung C. C., Seth A. C., Böker T., 2012, ApJ, 753, 38
Sepinsky J. F., Willems B., Kalogera V., Rasio F. A., 2007, ApJ, 667, 1170
Tejeda E., Rosswog S., 2013, MNRAS, 433, 1930 (TR)
van den Bosch R. C. E., Gebhardt K., Gültekin K., van de Ven G., van der Wel A., Walsh J. L., 2012, Nature, 491, 729
Wang J., Merritt D., 2004, ApJ, 600, 149
Zheng Z. et al., 2014, ApJ, 785, L23
Zhong J. et al., 2014, ApJ, 789, L2

APPENDIX A: DERIVATION OF THE TIDAL GRAVITATIONAL FIELD FOR THE TR POTENTIAL

In this appendix, we provide explicit expressions for the tidal tensor corresponding to the TR potential and quantify its departure from the exact relativistic result in Schwarzschild space–time. The

acceleration exerted on a given test particle under the TR potential is given by (Tejeda & Rosswog 2013)

$$\ddot{x}_i = -\frac{GM_{bh}x_i}{r^3}\left(1-\frac{r_s}{r}\right)^2 + \frac{r_s\dot{x}_i\,\dot{r}}{r(r-r_s)} - \frac{3}{2}\frac{r_sx_i\,\dot{\varphi}^2}{r}, \quad (A1)$$

where $x_i = \{x, y, z\}$ and r, $\dot{r}$ and $\dot{\varphi}$ should be taken as implicit functions of the Cartesian coordinates satisfying

$$r^2 = x^2 + y^2 + z^2, \quad (A2)$$

$$r\,\dot{r} = x\,\dot{x} + y\,\dot{y} + z\,\dot{z}, \quad (A3)$$

$$r^4\dot{\varphi}^2 = (x\,\dot{y} - y\,\dot{x})^2 + (x\,\dot{z} - z\,\dot{x})^2 + (z\,\dot{y} - y\,\dot{z})^2. \quad (A4)$$

We now consider a star approaching the central black hole. The centre of mass of the star is located at x_0 and follows, to a very good approximation, the trajectory of a free-falling test particle. We can compute the tidal forces acting on a fluid element located at a generic position x within the star by taking the Taylor series expansion of equation (A1) around x_0, i.e.

$$\ddot{x}_i = f_i(\boldsymbol{x}, \dot{\boldsymbol{x}}) \simeq f_i|_{(\boldsymbol{x}_0, \dot{\boldsymbol{x}}_0)} + (\boldsymbol{x} - \boldsymbol{x}_0)_j \left.\frac{\partial f_i}{\partial x_j}\right|_{(\boldsymbol{x}_0, \dot{\boldsymbol{x}}_0)}$$

$$+ (\dot{\boldsymbol{x}} - \dot{\boldsymbol{x}}_0)_j \left.\frac{\partial f_i}{\partial \dot{x}_j}\right|_{(\boldsymbol{x}_0, \dot{\boldsymbol{x}}_0)}, \quad (A5)$$

where the Einstein summation convention is used. Next we substitute $\xi = \boldsymbol{x} - \boldsymbol{x}_0$ into equation (A5) and find that, to first order in ξ and $\dot{\xi}$, the acceleration acting on a fluid element due to the central black hole as seen from the centre of mass of the star is given by

$$\ddot{\xi}_i = \xi_j C_{ij}|_{(\boldsymbol{x}_0, \dot{\boldsymbol{x}}_0)} + \dot{\xi}_j \widetilde{C}_{ij}|_{(\boldsymbol{x}_0, \dot{\boldsymbol{x}}_0)}, \quad (A6)$$

with the tidal tensors C_{ij} and $\widetilde{C}_{ij}$ given by

$$C_{ij} \equiv \frac{\partial f_i}{\partial x_j} = -\frac{GM_{bh}}{r^3}\left(1-\frac{r_s}{r}\right)^2\left[\delta_{ij} - \left(\frac{3\,r - 5\,r_s}{r-r_s}\right)\frac{x_i\,x_j}{r^2}\right]$$

$$+ \frac{r_s\dot{x}_i\,\dot{x}_j}{r^2(r-r_s)}\left[\delta_{ij} - \left(\frac{3\,r-2\,r_s}{r-r_s}\right)\frac{\dot{r}\,x_j}{r\,\dot{x}_j}\right]$$

$$- \frac{3\,r_s}{2\,r}\dot{\varphi}^2\left(\delta_{ij} - \frac{5\,x_i\,x_j}{r^2}\right) - \frac{3\,r_sx_i}{r^5}\left(x_jv^2 - r\,\dot{r}\,\dot{x}_j\right), \quad (A7)$$

$$\widetilde{C}_{ij} \equiv \frac{\partial f_i}{\partial \dot{x}_j} = \frac{r_s(r\,\dot{r}\,\delta_{ij} + x_j\,\dot{x}_i)}{r^2(r-r_s)} - \frac{3\,r_sx_i}{r^4}\left(r\,\dot{x}_j - \dot{r}\,x_j\right), \quad (A8)$$

where δ_{ij} is the Kronecker delta symbol and $v^2 = \dot{x}^2 + \dot{y}^2 + \dot{z}^2$.

Now we would like to compare the results in equations (A7) and (A8) with the corresponding exact relativistic expressions. It is customary to express the tidal tensor in Schwarzschild space–time by adopting the so-called Fermi normal coordinates centred on the approaching star (see e.g. Marck 1983; Brassart & Luminet 2010). Nevertheless, for consistency with the approach that we have adopted here, we need to calculate the tidal field using Schwarzschild coordinates (i.e. in the global reference frame centred on the black hole). The starting point is then the full-relativistic expression for the acceleration acting on a test particle in Schwarzschild space–time

$$\ddot{x}_i = -\frac{GM_{bh}x_i}{r^3}\left(1-\frac{r_s}{r}\right) + \frac{r_s\dot{x}_i\,\dot{r}}{r(r-r_s)} + \frac{r_sx_i\,\dot{r}^2}{2(r-r_s)r^2} - \frac{r_sx_i\,\dot{\varphi}^2}{r}. \quad (A9)$$

Following the same steps leading to equation (A6), it is found that the tidal tensors are now given by

$$C_{ij}^S = -\frac{GM_{bh}}{r^3}\left(1-\frac{r_s}{r}\right)\left[\delta_{ij} - \left(\frac{3\,r-4\,r_s}{r-r_s}\right)\frac{x_i\,x_j}{r^2}\right]$$

$$+ \frac{r_s\dot{x}_i\,\dot{x}_j}{r^2(r-r_s)}\left[\delta_{ij} + \frac{\dot{r}\,x_i}{r\,\dot{x}_i} - \left(\frac{3\,r-2\,r_s}{r-r_s}\right)\frac{\dot{r}\,x_j}{r\,\dot{x}_j}\right]$$

$$+ \frac{r_s\dot{r}^2}{2\,r^2(r-r_s)}\left[\delta_{ij} - \left(\frac{5\,r-4\,r_s}{r-r_s}\right)\frac{x_i\,x_j}{r^2}\right]$$

$$- \frac{r_s}{r}\dot{\varphi}^2\left(\delta_{ij} - \frac{5\,x_i\,x_j}{r^2}\right) - \frac{2\,r_sx_i}{r^5}\left(x_jv^2 - r\,\dot{r}\,\dot{x}_j\right), \quad (A10)$$

$$\widetilde{C}_{ij}^S = \frac{r_s(r^2\dot{r}\,\delta_{ij} + x_j\,x_i\,\dot{r} + r\,x_j\,\dot{x}_i)}{r^3(r-r_s)} - \frac{2\,r_sx_i}{r^4}\left(r\,\dot{x}_j - \dot{r}\,x_j\right), \quad (A11)$$

where the superscript 'S' is used to indicate that the quantity has been calculated in Schwarzschild space–time.

The eigenvalues of the tidal tensor C_{ij} give pertinent physical information about the amount of compression or expansion that the stellar matter experiences due to the black hole along the direction of the principal axes of the tidal tensor. These eigenvalues can be found by following the standard procedure of diagonalizing C_{ij}. In particular, if we choose a global reference frame XYZ such that the trajectory followed by the centre of mass of the star coincides with the XY plane (which is always possible due to the spherical symmetry of the present problem), the corresponding eigenvalues are given by

$$\lambda_{1,2} = \frac{1}{2}\left[C_{11} + C_{22} \pm \sqrt{(C_{11}+C_{22})^2 - 4(C_{11}C_{22}-C_{12}C_{12})}\right],$$
$$\lambda_3 = C_{33}. \quad (A12)$$

Equivalent expressions are found for λ_i^S by substituting C_{ij}^S instead of C_{ij} into equation (A12).

In Fig. A1, we compare the eigenvalues in equation (A12) with the corresponding relativistic values λ_i^S for a parabolic trajectory with $h = 5\,r_sc$ (which represents a $\beta \simeq 1$ encounter between a solar-type star and a $10^6\,M_\odot$ black hole). As a reference to
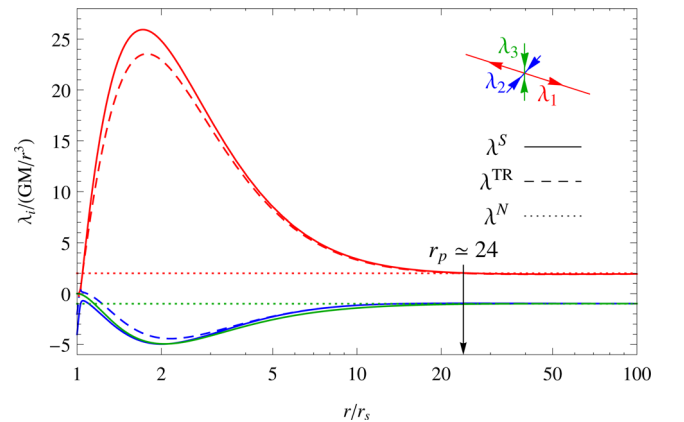

Figure A1. Comparison of the eigenvalues of the tidal tensor as obtained in Schwarzschild space–time (solid lines), for the TR potential (dashed lines) and for the Newtonian potential (dotted lines). In this case, we have taken a parabolic encounter with $h = 5\,r_sc$, corresponding to a $\beta \simeq 1$ encounter between a solar-type star with a $10^6\,M_\odot$ central black hole.
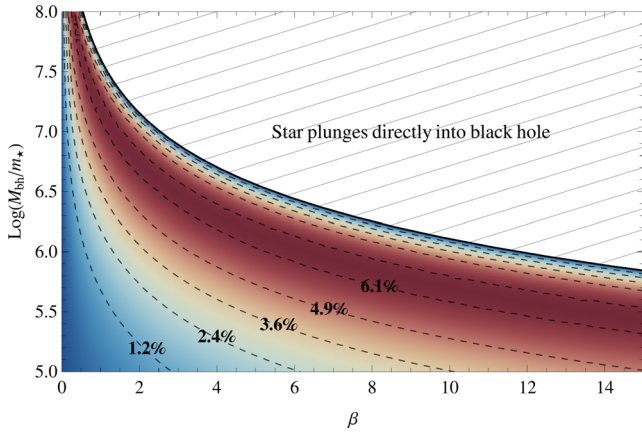
Figure A2. Contours of the maximum relative error with which the eigenvalue of the tidal tensor λ_1 (equation A12) reproduces the exact relativistic value λ_1^S as a function of the impact parameter β and the mass ratio $q = M_{bh}/m_\star$.

illustrate the importance of relativistic effects, we have also plotted the corresponding Newtonian values (Brassart & Luminet 2008)

$$\lambda_1^N = \frac{2\,GM_{bh}}{r^3}, \qquad \lambda_2^N = \lambda_3^N = -\frac{GM_{bh}}{r^3}. \tag{A13}$$

In this figure and for any other parabolic encounter, the eigenvalue λ_3 coincides exactly with the corresponding relativistic result. More specifically, for a parabolic trajectory with angular momentum h, it is found that

$$\lambda_3 = \lambda_3^S = -\frac{GM_{bh}}{r^3}\left(1 - \frac{r_s}{r}\right)^2\left(1 + \frac{3\,h^2}{r^2c^2}\right). \tag{A14}$$

This means that tidal compression along the vertical direction is reproduced exactly by the TR potential for parabolic encounters. On the other hand, it is also apparent from Fig. A1 that the eigenvalues λ_1 and λ_2 provide a good approximation to the exact relativistic values. In a practical simulation, the maximum departure of the tidal field corresponding to the TR potential from the relativistic result is reached at the periapsis of the incoming trajectory. In Fig. A2, we show the contours of the maximum relative error for λ_1 (i.e. $(\lambda_1^S - \lambda_1)/\lambda_1^S$) as a function of the impact parameter β and the mass ratio $q = M_{bh}/m_\star$. From this figure, we see that expansion due to the tidal tensor is reproduced by the TR potential with a precision better than 6.4 per cent. Finally, the relative error for λ_2 at periapsis was found to be consistently zero within machine precision ($\approx 10^{-15}$) for the parameter values shown in Fig. A2. This appears to contradict

the fact that λ_2^{TR} deviates from λ_2^S at $r \sim 2r_s$ in Fig. A1, but note that the maximum error occurs at pericentre, which in Fig. A1 is at $r \sim 24r_s$ and that the curves shown there will change with β.

APPENDIX B: THE ROCHE POTENTIAL FOR NON-CIRCULAR ORBITS

The Roche lobe is defined in the context of the so-called restricted three-body problem, where a test particle moves in the potential of two orbiting masses. It is bounded by the critical equipotential surface of the effective potential $\Phi_{eff}(\mathbf{r})$, incorporating inertial forces in the coordinate frame that is comoving and corotating with the star (Sepinsky et al. 2007). In such a non-inertial frame, the expression for the effective potential reads

$$\Phi_{eff}(\mathbf{r}) = \Phi_*(\mathbf{r}) + \Phi_{bh}(\mathbf{r}) - (\mathbf{r} - \mathbf{r}_*) \cdot \nabla_* \Phi_{bh}(\mathbf{r}_*)$$
$$-\frac{1}{2}|\omega(\mathbf{r}) \times (\mathbf{r} - \mathbf{r}_*)|^2. \tag{B1}$$

Here, $\mathbf{r}_*$ is the current instantaneous position of the centre of mass (CoM) of the star, ∇_* is the gradient with respect to $\mathbf{r}_*$, $\omega(\mathbf{r})$ is the angular velocity at the position $\mathbf{r}$. The first two terms in this expression, $\Phi_*(\mathbf{r})$ and $\Phi_{bh}(\mathbf{r})$, represent the gravitational potentials of the star and the black hole, respectively; in our simulations, the former is computed with the tree, while the latter can be either Φ_N or Φ_{TR}. The third term appears because our reference frame is comoving with the star. It produces uniform acceleration, equal and opposite to the one of the CoM of the star. The last term is the centrifugal potential due to stellar rotation.

If we use point particle Newtonian potentials for the black hole and the star, the effective potential becomes

$$\Phi_{eff}(\mathbf{r}) = -\frac{Gm_*}{r} - \frac{GM_{bh}}{r} - \frac{GM_{bh}}{r_*^3}\,\mathbf{r}_* \cdot (\mathbf{r} - \mathbf{r}_*)$$
$$-\frac{1}{2}|\omega(\mathbf{r}) \times (\mathbf{r} - \mathbf{r}_*)|^2. \tag{B2}$$

The choice of angular velocity ω in the effective potential depends on how the star is rotating and is not very clearly defined in the post-disruption phase. Therefore, in Fig. 2, for the contours of $\Phi_{eff}(\mathbf{r})$ (dashed black lines) we adopt an average angular velocity $\langle\omega\rangle = \frac{1}{N_{part}}\sum_a \omega_a$ (where a is the particle index), while for the colours of individual particles we use the values of the individual angular velocities ω_a.

This paper has been typeset from a TEX/LATEX file prepared by the author.